Meteorology and Atmospheric Physics (2019) 131:807–825
https://doi.org/10.1007/s00703-018-0607-4

ORIGINAL PAPER

Analysis of the convective characteristics during the mutual evolution of an inverted trough/low vortex and its induced rainstorm over the northeastern Sichuan basin, China

Yongren Chen[1,2,3] · Yueqing Li[1,3] · Dongmei Qi[1,3]

Received: 2 October 2017 / Accepted: 20 April 2018 / Published online: 27 April 2018

Abstract
Based on a variety of ground-based and satellite-derived observational data, we studied a flood-rainstorm event that occurred over northeastern Sichuan, China, from the 8th to the 14th of September 2014. Four periods of mesoscale convective system (MCS) activity were found during a mutual evolution process of an 850-hPa basin inverted trough (BIT) and 850-hPa basin low vortex (BLV). Among them, the first three periods occurred in an alternating evolution of the BIT and BLV (called the first stage), and then, the fourth period was stimulated by continuous activity of the BLV (called the second stage). During the first stage, MCSs enhanced (weakened) under the situation of the BIT (BLV), and then during the second stage MCSs developed to their strongest levels. Further analysis of the reasons behind the enhancement and weakening of MCSs revealed an obvious characteristic of upper level (lower level) positive (negative) divergence in the BIT situation of the first stage and BLV situation of the second stage. By comparison, under the BLV situation of the first stage, the vertical helicity was larger in the upward airflow of the zonal circulation, and the direction of the wet Q-vector was toward the ascending airflow in the vertical direction. In the horizontal direction, the negative divergence of the wet Q-vector corresponded to the position of water vapor flux convergence. In addition, in the early development of convection, sounding data showed a humidity profile of dry upper and wet lower levels, as well as a larger value of convective available potential energy, which triggered convective activity under the favorable dynamic conditions of atmosphere. When the above characteristics weakened, the convective activity also weakened. Therefore, the formation of multiple convective systems was closely related to the adjustment in atmospheric conditions around the BIT and BLV.

1 Introduction

The Tibetan Plateau, China, is the world's highest altitude land area and, owing to its particular topography and the unique thermodynamic characteristics of the overlying atmosphere, often gives rise to the occurrence of mesoscale vortices over its main body leeward slope in the east (Tao and Ding 1981). Among these weather systems, the Tibetan Plateau vortex (TPV), at 500 hPa (Shen et al. 1986; Wang 1987; Wang and Orlanski 1987; Yu and Gao 2009; Yu et al. 2014, 2016), and southwest China vortex (SWCV) (Lu 1986; Kuo et al. 1986, 1988), at 700 hPa and below, are the most representative. In summer, due to the frequent activity of mesoscale vortices over and moving away from the Tibetan Plateau, flood-level rainstorm events often occur over the Sichuan basin (SB) and other regions along the Yangtze River; for example: the occurrence of heavy rain events over the SB in mid-July 1981 (Kuo et al. 1988); heavy rainfall and disastrous flooding of the Yangtze River in 1998 (Bei et al. 2002; Cheng et al. 2001); a long-term heavy rainfall event over south China in mid-June 2008, which was closely related to SWCV activity (Fu et al. 2011; Chen et al. 2015); the heavy rainstorm of 21–22 July 2012 in the eastern part of the Sichuan–Chongqing basin—also closely related to the SWCV (Chen and Li 2013); and an extreme rainstorm in the eastern SB, stimulated by interaction between the SWCV

Responsible Editor: M. Telisman Prtenjak.

✉ Yongren Chen
yr20060004@163.com

[1] Institute of Plateau Meteorology, China Meteorological Administration, Chengdu 610072, Sichuan, China

[2] Sichuan Provincial Meteorological Observatory, Chengdu 610072, Sichuan, China

[3] Heavy Rain and Drought-Flood Disasters in Plateau and Basin Key Laboratory of Sichuan Province, Chengdu 610072, China

and TPV (Cheng et al. 2016). These cases demonstrate the importance of TPV and SWCV activity for the occurrence of strong precipitation. Therefore, understanding the structure and developmental mechanisms of these vortices, as well as successfully forecasting their tracks, has long been a key concern of meteorological research in China, and many studies have been carried out in this regard, achieving some fruitful results in aiding our understanding of these vortex systems (Wu and Chen 1985; Wang 1987; Chen and Luo 2003; Wang and Gao 2003; Li et al. 2011, 2014a, b, c; Yu and Gao 2009). Most recently, several studies have used the latest data to reveal some interesting new facts related to these two vortices (Xiang et al. 2013; Li and Deng 2013; Wang and Tan 2014; Li et al. 2014c; Lin 2015; Cheng et al. 2016; Feng et al. 2016; Ni et al. 2017). In fact, the TPV and SWCV belong to categories of mesoscale vortices of different heights (Yu et al. 2016). Plus, compared to the TPV, the spatial range for SWCV formation is greater, occurring not only over the eastern leeward slope of the Tibetan Plateau, but also over the SB. When an SWCV forms over the SB, it is called a basin low vortex (BLV) (Lu 1986).

The BLV and basin inverted trough (BIT) are common weather systems that induce rainstorms over Sichuan, often appearing in the 850-hPa wind field. Because of the unique terrain of the SB, and other factors, and coupled with the limitations (i.e., sparseness) of observational data (Li et al. 2015), to track and identify these systems are more difficult compared with the same tasks for the SWCV. Sometimes, a BLV is not a completely closed circulation system, like a typhoon or high-altitude cold vortex, so its closed contours are often not analyzed and only display the cyclonic flow field. If the situation is one of northeasterly winds in the western SB and southeasterly winds in the eastern SB, this cyclonic flow field is referred to as the BIT (Li and Gao 2007). Under favorable conditions, some BITs will evolve into BLVs, or both BLVs and BITs will appear alternately, persisting for around 3–5 days and resulting in continuous rainy weather or even rainstorm events in the SB. Among the previous studies, few have revealed the relationships between the BLV and BIT. In fact, sometimes, a BIT will evolve into a BLV. However, the BLV and its impact on the heavy rain in weather forecasts is generally of more concern, with the relationship between the BIT and BLV in the early stages of development, and their alternating evolution, in the context of the impacts of the rainstorm, often ignored.

The rainstorm that occurred during 8–14 September 2014 in the eastern SB was not only affected by stable upper level weather systems, but was also closely related to the alternating evolution of an 850-hPa BLV and BIT. According to the 12-h sounding wind field data, the 850-hPa wind over the SB was a BLV at 0000 UTC 8 September, 0000 UTC 9 September, 0000 UTC 10 September, 0000 UTC 11 September, and 0000 UTC 12 September to 0000 UTC 14 September; but a BIT at 1200 UTC 8 September, 1200 UTC 9 September, 1200 UTC 10 September, and 1200 UTC 11 September. In addition, there was an alternating evolution between the BLV and BIT from 1200 UTC 8 September to 0000 UTC 12 September (referred to as the first stage of the rainstorm), and then a maintenance of a BLV from 0000 UTC 12 September to 0000 UTC 14 September (referred to as the second stage of the rainstorm). From the low-level atmospheric situation, the 850-hPa wind changed significantly in the rainstorm area and there was a mutually alternating evolution between the 850-hPa BIT and BLV. The activities of mesoscale convective systems (MCSs) were also obvious, developing under the BIT situation but weakening under the BLV situation in the first stage of the rainstorm. In the second stage, MCSs developed strongly and lasted for around 18 h.

Compared with the real situation, the forecast of the above-mentioned rainstorm case featured some deviations in terms of the magnitude of precipitation at the beginning and end of the event, as well as the heavy rainstorm area during the second stage. From the perspective of trying to understand why the evolution of such BIT and BLV systems can be so inaccurately predicted, in the present study, we investigated the possible causes of this rainstorm process and sought to provide results that can act as a reference for similar rainstorm forecasts in the future. Following this introduction, Sect. 2 describes the data and methods; Sect. 3 analyzes the rainstorm distribution and its impact systems; Sect. 4 analyzes characteristics of four periods of convective cloud in the rainstorm; Sect. 5 explains the differences in conditions between the BIT and BLV; and Sect. 6 concludes the study.

2 Data and methods

The data used in this study were as follows:

(1) Sounding observational data at 0000 UTC and 1200 UTC;
(2) FNL (final) operational global analysis data of the National Centers for Environmental Prediction (NCEP), with a spatial resolution of $1^\circ \times 1^\circ$ and temporal resolution of 6 h (0000 UTC, 0600 UTC, 1200 UTC, and 1800 UTC each day; hereafter referred to as NCEP_fnl; http://rda.ucar.edu/datasets/ds083.2/);
(3) Brightness temperature (Tb) data from the thermal IR channel (10.5–12.5 micron) of FY2D geostationary weather satellite provided by the Meteorological Satellite Center of the China Meteorological Administration, with a spatial resolution of $0.1^\circ \times 0.1^\circ$ grids (http://www.nsmc.org.cn/NSMC/Home/Index.html);

(4) Observational precipitation data provided by China Meteorological Administration;
(5) Forecast data, mainly from the European Centre for Medium-Range Weather Forecasts.

The methods used included non-geostrophic wet Q-vector diagnostics (Davis-Jones 1991; Zhang 1998), and vertical helicity (Lilly 1986; Lu and Gao 2003). In the P-coordinate system, the wet Q-vector is written as follows:

$$\vec{Q}^* = Q_x^*\vec{i} + Q_y^*\vec{j}, \tag{1}$$

$$Q_x^* = 1/2\left[f\left(\frac{\partial v}{\partial p}\frac{\partial u}{\partial x} - \frac{\partial u}{\partial p}\frac{\partial v}{\partial x}\right) - h\frac{\partial \vec{V}_h}{\partial x}\cdot\nabla\theta - \frac{\partial}{\partial x}\left(\frac{LR\omega}{C_pP}\frac{\partial q_s}{\partial p}\right)\right], \tag{2}$$

$$Q_y^* = 1/2\left[f\left(\frac{\partial v}{\partial p}\frac{\partial u}{\partial y} - \frac{\partial u}{\partial p}\frac{\partial v}{\partial y}\right) - h\frac{\partial \vec{V}_h}{\partial y}\cdot\nabla\theta - \frac{\partial}{\partial y}\left(\frac{LR\omega}{C_pP}\frac{\partial q_s}{\partial p}\right)\right], \tag{3}$$

where $\vec{V}_h$ and $\nabla\theta$ are two-dimensional vectors; $h = \frac{R}{p}\left(\frac{p}{1000}\right)^{\frac{R}{C_p}}$; u and v are the zonal and meridional components of $\vec{V}_h$, respectively; θ is the potential temperature, p is the pressure, and the Coriolis parameter f is assumed to be constant. Equations (2) and (3) show that the wet Q-vector depends on the differential effects of horizontal and vertical wind shear, the product of the horizontal wind gradient, the potential temperature gradient, and the non-adiabatic effect.

The helicity is defined as follows:

$$H = \vec{V}\cdot(\nabla\times\vec{V}) = \underbrace{u\left(\frac{\partial w}{\partial y} - \frac{\partial v}{\partial z}\right)}_{(a)} + \underbrace{v\left(\frac{\partial u}{\partial z} - \frac{\partial w}{\partial x}\right)}_{(b)} + \underbrace{w\left(\frac{\partial v}{\partial x} - \frac{\partial u}{\partial y}\right)}_{(c)}, \tag{4}$$

where $\vec{V} = u\vec{i} + v\vec{j} + w\vec{k}$; $\nabla\times\vec{V}$ is three-dimensional vorticity; (a) is x-helicity, (b) is y-helicity, and (c) is z-helicity (also called vertical helicity, VH):

$$\mathrm{VH} = w\left(\frac{\partial v}{\partial x} - \frac{\partial u}{\partial y}\right) \cong -\frac{1}{\rho g}\omega\left(\frac{\partial v}{\partial x} - \frac{\partial u}{\partial y}\right). \tag{5}$$

Here, ω is the vertical velocity of the P-coordinate system, w is the vertical velocity of the Z-coordinate system, ρ is atmospheric density, and g is the gravitational acceleration constant.

3 Rainstorm distribution and its impact systems

Based on the data of hourly rainfall and lightning observations (figure omitted), the most prominent features of the rainstorm were a relatively long duration, dense lightning activity, high precipitation efficiency, a rainstorm area that was relatively concentrated, and a level of accumulative precipitation that remained high throughout in the whole process. Figure 1 shows the 24-h accumulative precipitation recorded by automatic weather stations and Table 1 shows number of stations (SN) for each category of 24-h accumulated precipitation, from which it can be seen that, from 1200 UTC 8 September to 1200 UTC 9 September, the rainstorm occurred at Bazhong, Guangyuan, Nanchong, and Suining. The SN recording above 50 mm reached 215 and the maximum precipitation amount was 258.9 mm. From 1200 UTC 9 September to 1200 UTC 10 September, the rainstorm area was located over Bazhong and Guangyuan, with an SN of 66 for above 50 mm, and a maximum of 242.9 mm. From 1200 UTC 10 September to 1200 UTC 11 September, the rainstorm area was located over Bazhong, Nanchong, Guangyuan, and Suining, with the SN reaching 223 for above 50 mm, and a maximum of 295.3 mm. From 1200 UTC 11 September to 1200 UTC 12 September, the rainstorm was concentrated over Bazhong, Nanchong, Ya'an, Leshan, Neijiang, and Zigong, with the SN reaching 315 for above 50 mm, and the maximum was 234 mm. From 1200 UTC 12 September to 1200 UTC 13 September, the rainstorm area was concentrated over Dazhou, Guang'an, Bazhong, and Nanchong, with the SN reaching 494 for above 50 mm, and the maximum was 295.1 mm. From 1200 UTC 13 September to 1200 UTC 14 September, the SN for both amounts markedly reduced as the rainstorm came toward its end. During the course of this rainstorm event, in addition to the range of precipitation being narrow on the second and third days, other prominent features included the range being much larger on the other 4 days and the rainstorm being characterized by a long duration and a concentrated area.

Usually, rainstorms of long duration in this region are stimulated directly by a precipitation system against the background of a subtropical high ridge, long trough, shear line, static front, and large-scale low-pressure systems. By summarizing the circulation characteristics at 500, 700, and 850 hPa (Fig. 2), the atmospheric situation of the present rainstorm case had the following characteristics:

(1) The circulation situation of "west-low–east-high" at the middle level was maintained over the Sichuan for about a week, which constituted the background against which this persistent rainstorm formed. During the precipitation process, the 500-hPa western Pacific subtropical high (WPSH; Duan et al. 2017) stabilized near 108°–109°E, and westerly troughs frequently moved over its northwest side. The configuration of troughs and the WPSH formed an "east-high/west-low" circulation background mode and, from the evolutionary distribution at 12-h intervals, precipitating clouds mainly were located over the Sichuan and there were

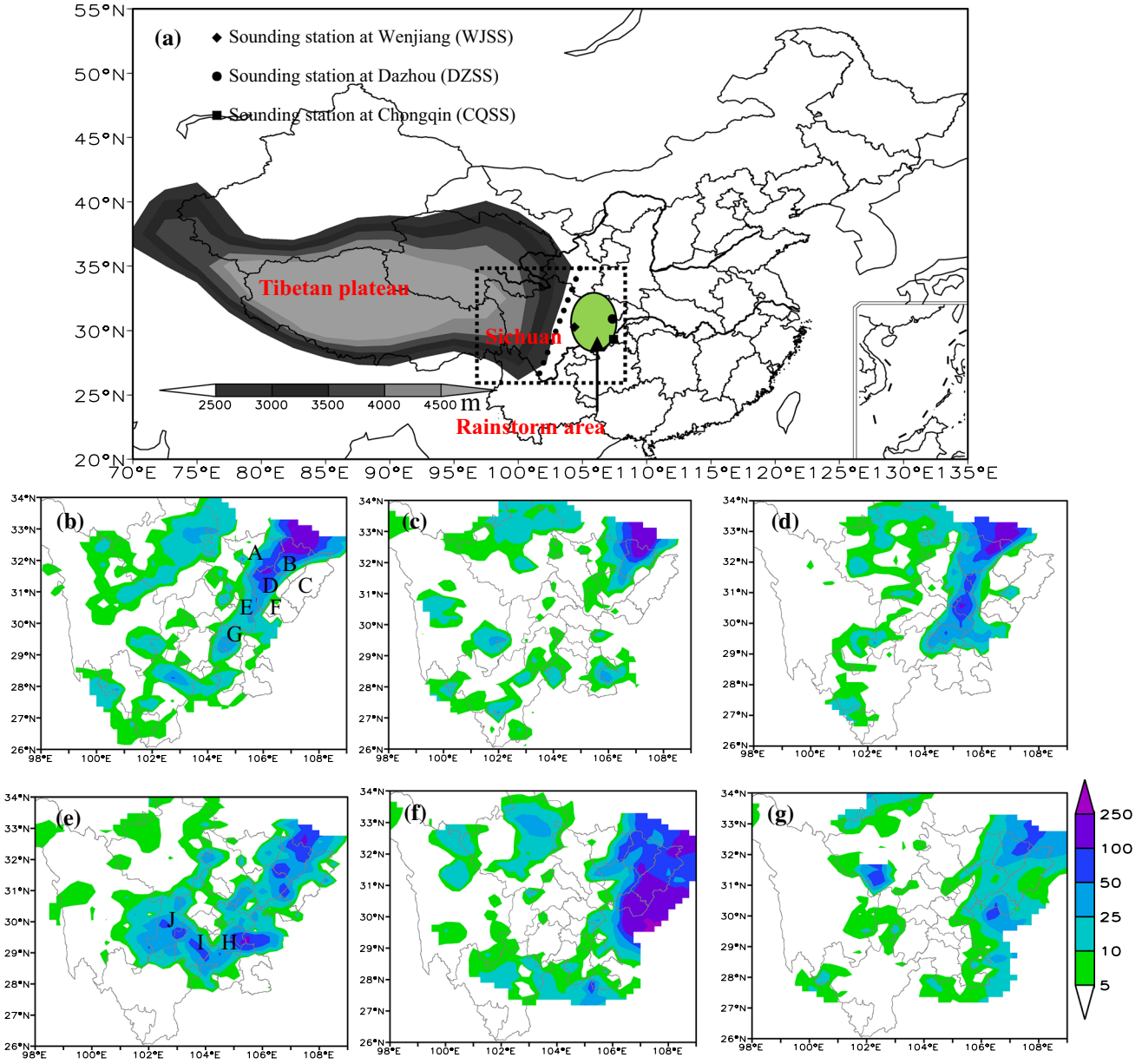

Fig. 1 Rainstorm location (**a**) and 24-h accumulative precipitation distribution (**b**–**g**) from 1200 UTC 8 September to 1200 UTC 14 September 2014 (units: mm): **b** 1200 UTC 8 September to 1200 UTC 9 September; **c** 1200 UTC 9 September to 1200 UTC 10 September; **d** 1200 UTC 10 September to 1200 UTC 11 September; **e** 1200 UTC 11 September to 1200 UTC 12 September; **f** 1200 UTC 12 September to 1200 UTC 13 September; **g** 1200 UTC 13 September to 1200 UTC 14 September. Zones A–J: Guangyuan, Bazhong, Dazhou, Nanchong, Suining, Guang'an, Neijiang, Zigong, Leshan, and Ya'an

convective systems with Tb values of less than − 52 °C developing in the cloud band.

(2) In the low-level wind field, there was a branch of southwest airflow of 6–14 m s^{-1} from Yunnan to the basin at 700 hPa that configured with northerly winds of 6–8 m s^{-1} in southern Gansu to form a shear line, thus providing favorable conditions for water vapor convergence. At 850 hPa, there was a cyclonic flow field in the SB, but the rotational characteristics of the wind changed noticeably, revealing two main forms of BIT and BLV circulation, such as from 1200 UTC 8 September to 0000 UTC 12 September. The 850-hPa wind field showed a mainly alternating evolution of the BIT (at night) and BLV (during daytime), corresponding to the strong precipitation being mainly concentrated in the BIT period (figure omitted). From 1200 UTC 12 September to 0000 UTC 14 September, a deeper BLV was maintained, which not only existed at 850 hPa but

Table 1 Number of stations for each category of 24-h accumulated precipitation

Statistical period (1200 UTC–1200 UTC)	Number of stations (SN)		
	50.0 –99.9 mm	100.0–250.0 mm	The max (mm)
8–9 September	161	54	258.9
9–10 September	46	24	249.2
10–11 September	175	48	295.3
11–12 September	261	54	234.0
12–13 September	267	227	295.1
13–14 September	42	0	84.5

also extended to 700 hPa and stimulated the strongest spell of precipitation throughout the whole process. Therefore, from the observed systems of impact—mainly in the background of the 500-hPa WPSH and westerly troughs—the MCSs of this event developed strongly in the BLV and BIT, and then created the rainstorm. Although the BLV persisted throughout the entire precipitation process, the strong precipitation of the first stage was mainly caused by the adjustment from BIT to BLV, whilst the second stage was caused by the development of the BLV.

In the forecast, only moderate-to-strong rainfall was shown over the northeastern part of Sichuan, and at 1200 UTC 8 September, before the occurrence of the rainstorm, the low-level wind field of the sounding showed a BIT, with the 700-hPa southwesterly wind reaching 4–10 m s^{-1} but not the low-level jet. Although the satellite image showed that there was a clear convective cloud belt from the Plateau of western Sichuan (PWS) to the north of the SB, from the subsequent evolution (Fig. 2a), the MCSs that created the rainstorm were caused by the growth of several small convective systems near the BIT and moved northward to the rain area, while the cloud belts over the PWS weakened. Therefore, based on the forecast field and sounding situation, only moderate-to-strong rain was predicted over the northeastern part of the SB, and the lack of analysis of the MCSs near the BIT led to the leakage of the rainstorm. During 9–11 September, because the atmospheric circulation was similar to that of 8 September, it was better to forecast the rainstorm during this period. In the forecast from 0000 UTC 12 September to 0000 UTC 14 September, such as the atmospheric circulation at 1200 UTC 12 September, whilst the satellite image (Fig. 2i) showed that there were cloud belts around the SWCV, in the subsequent evolution only the MCSs that were located in the east of the SWCV developed strongly, which represented a significant deviation between the forecast and the real situation.

Therefore, we can see that forecasting this rainstorm was a difficult task. To help alleviate the difficulties for similar cases in the future, we next analyzed the possible causes of the rainstorm in terms of the convective activity, configuration of weather systems, diagnosis of physical quantities, the sounding structure, and so on.

4 Characteristics of four periods of convective cloud in the rainstorm

The MCSs that develop near mesoscale vortices are usually the cause of the associated rainstorms (Schumacher and Johnson 2005, 2008; Sun et al. 2010; He et al. 2016; Chen and Li 2013, Chen et al. 2015). In the rainstorm process of the present study, the activity of MCSs was obvious and showed phase changes. Using the hourly Tb satellite data to analyze the convective activity, there were four periods of MCS activity during this process, three of which involved the alternating evolution of the BIT and BLV, and the fourth was influenced by a deep SWCV. Figures 3, 4, 5 show the distribution of Tb during the alternating evolution of the BIT and BLV. In the first period of activity (Fig. 4), when the BIT was evolving toward the BLV, there were MCSs in the northern part of the PWS and SB at 1600 UTC 8 September, with Tb values of less than − 60 °C in the cold cloud zone where the convective systems of region A were born. In the subsequent evolution, to 1900 UTC 8 September, old convective systems of the PWS gradually weakened, and newly born convective systems developed in the SB to form larger MCSs. The horizontal scale of the MCSs in region A was larger than 100 km (β-scale characteristic) and had moved to the north of the SB by 2100 UTC 9 September. After 0000 UTC 9 September was the period when the BLV evolved toward the BIT, in which the MCSs gradually weakened up to 0500 UTC 9 September. The cold cloud area of the convective systems had greatly reduced and disappeared by 0700 UTC 9 September, bringing the MCS activity of the first period to an end. The second period of convective activity developed from an isolated cloud. At 1200 UTC 10 September, MCSs generated in the middle part of the SB (figure omitted) and became middle β-scale systems with Tb values of less than − 60 °C. The area of cold cloud then grew and moved northward and, from 1900 UTC 10 September to 1200 UTC 10 September, the MCSs strengthened. They then weakened after 0000 UTC 11 September and, by 0500 UTC 11 September, the cold cloud area of the MCSs had disappeared and this second period of convection came to a close. The third period of convection, similar to the first period, was stimulated by the development of several small convective clouds merging in the SB. At 1900 UTC 11 September, the MCSs became strong, before weakening—especially so (i.e., at a fast rate) after 0000 UTC 12 September. It is clear

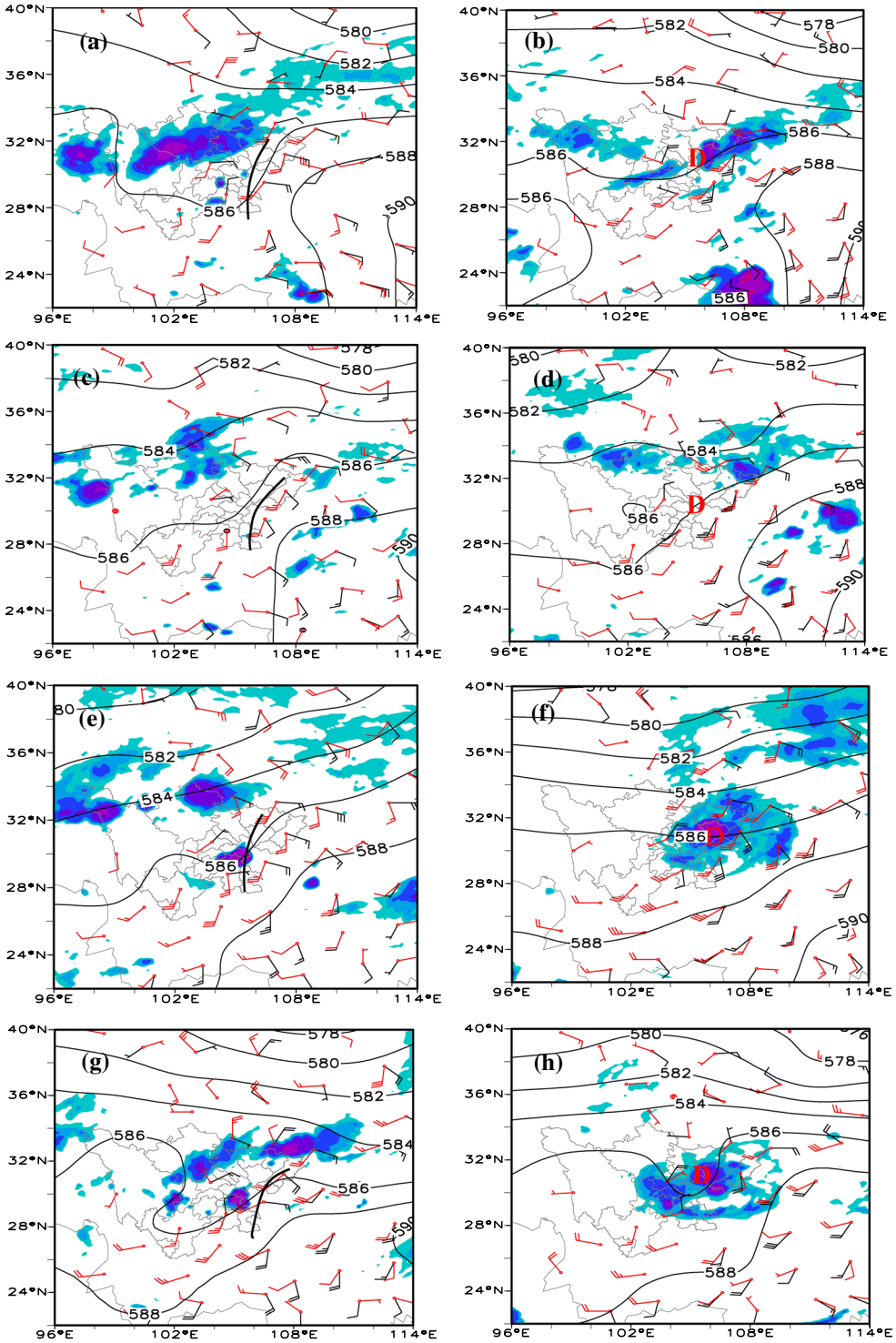

Fig. 2 500-hPa geopotential height field (contours; units: gpdam), 700-hPa (red), and 850-hPa (black) wind vectors (units: m s^{-1}), and Tb (shaded; units: °C). Solid line: 850-hPa BIT; D: 850-hPa BLV: **a** 1200 UTC 8 September; **b** 0000 UTC 9 September; **c** 1200 UTC 9 September; **d** 0000 UTC 10 September; **e** 1200 UTC 10 September; **f** 0000 UTC 11 September; **g** 1200 UTC 11 September; **h** 0000 UTC 12 September; **i** 1200 UTC 12 September; **j** 0000 UTC 13 September; **k** 1200 UTC 13 September; and **l** 0000 UTC 14 September

that these three periods of convective activity basically followed a pattern, whereby there was development under the BIT situation, but weakening under the BLV situation. In addition, the life cycles of the MCSs reached 12 h, and the horizontal scale of Tb values being less than −60 °C was between 100 and 200 km. Given that the process of the BIT (BLV) evolving toward the BLV (BIT) took place mainly at night (during the day), corresponding to enhancement (weakening) of the associated MCSs, it is clear that there was a prominent pattern of diurnal variation related to the three periods of convective activity.

Figure 6 shows the Tb distribution for the fourth period of convection, whose development was closely related to SWCV activity. At 1600 UTC 12 September, there were

Fig. 2 (continued)

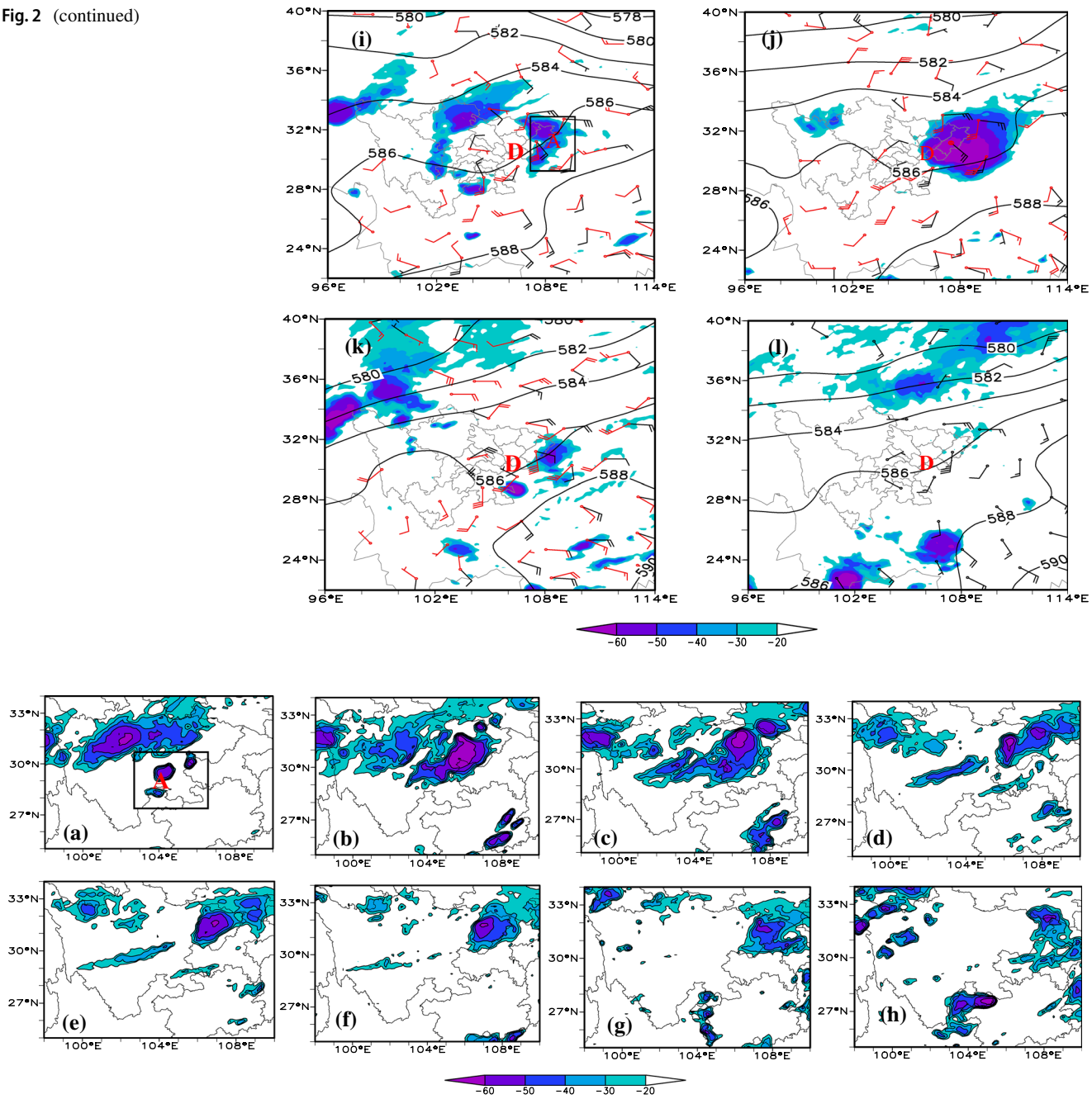

Fig. 3 Tb distribution in the first period of MCS activity (units: °C) (**a**–**d** evolution from the BIT to BLV; **e**–**h** evolution from the BLV to BIT) at **a** 1600 UTC 8 September, **b** 1900 UTC 8 September, **c** 2100 UTC 8 September, **d** 0000 UTC 9 September, **e** 0200 UTC 9 September, **f** 0500 UTC 9 September, **g** 0700 UTC 9 September, and **h** 1000 UTC 9 September

MCSs around the SWCV manifesting in the shape of a hollow circle. The MCSs of largest area were in region D, where the Tb values were less than − 60 °C. In the subsequent evolution, to 1900 UTC 12 September, the MCSs of region D that were direct rainstorm systems strengthened, whilst the rest of the clouds weakened, with the MCSs developing most strongly and reaching their most exuberant period by 2100 UTC 12 September. They then weakened after 0500 UTC 13 September. Compared with the three periods of convective activity in the first stage, this was the longest MCS episode and the SN for induced rainstorms was the highest. In addition, the strong MCS stage was mainly concentrated in both the early and later morning hours, so the diurnal variation was not as prominent compared with the previous three periods of convective activity.

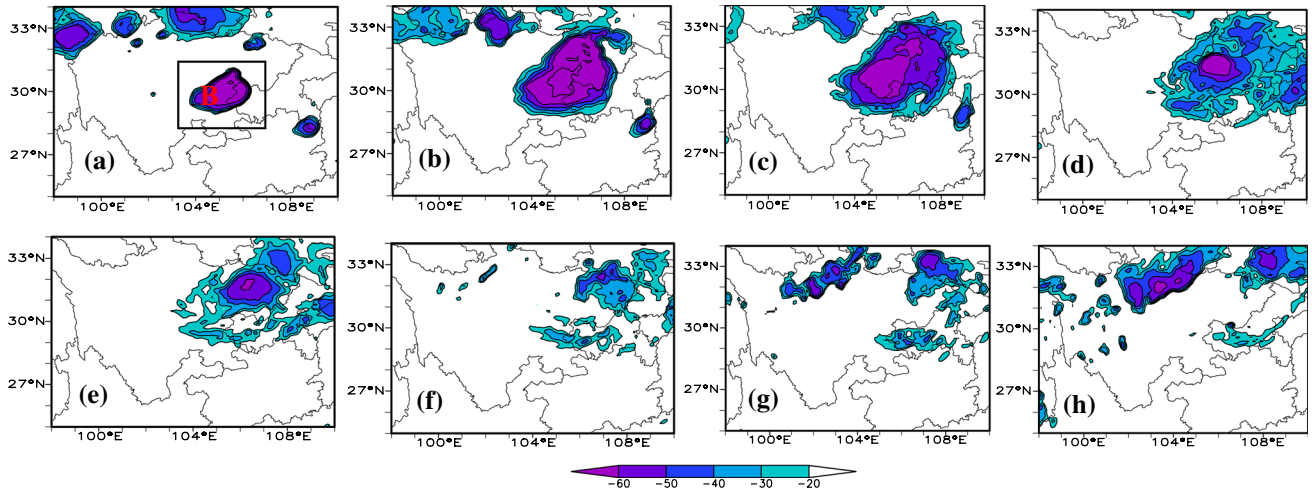

Fig. 4 Tb distribution in the second period of MCS activity (units: °C) (**a**–**d** evolution from BIT to BLV; **e**–**h** evolution from BLV to BIT) at **a** 1600 UTC 10 September, **b** 1900 UTC 10 September, **c** 2100 UTC 10 September, **d** 0000 UTC 11 September, **e** 0200 UTC 11 September, **f** 0500 UTC 11 September, **g** 0700 UTC 11 September, and **h** 1000 UTC 11 September

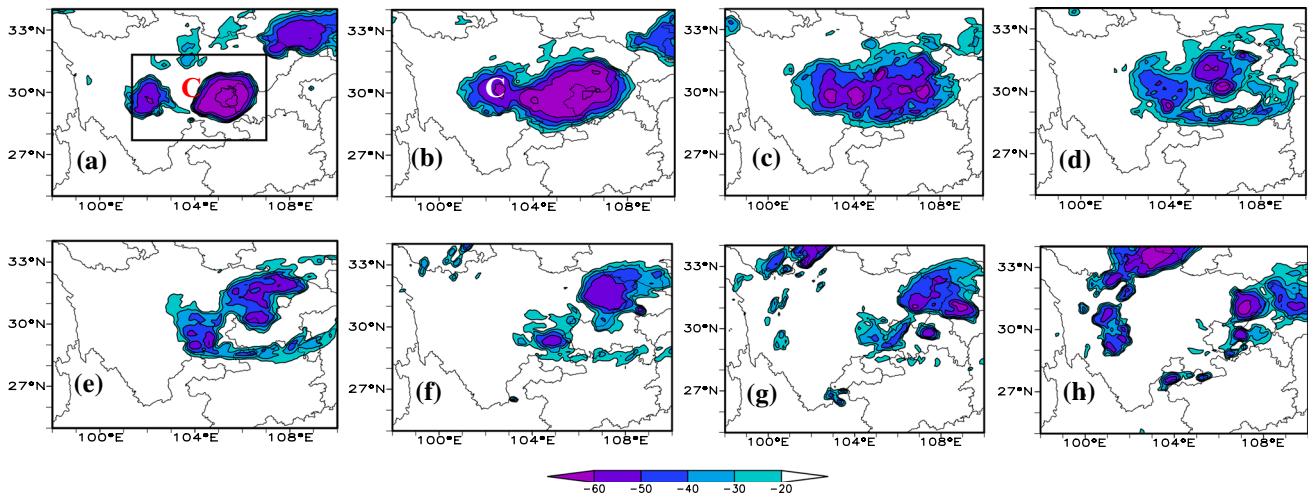

Fig. 5 Tb distribution in the second period of MCS activity (units: °C) (**a**–**d** evolution from BIT to BLV; **e**–**h** evolution from BLV to BIT) at **a** 1600 UTC 11 September, **b** 1900 UTC 11 September, **c** 2100 UTC 11 September, **d** 0000 UTC 12 September, **e** 0200 UTC 12 September, **f** 0500 UTC 12 September, **g** 0700 UTC 12 September, and **h** 1000 UTC 12 September

Figure 7 shows the vorticity, divergence, and vertical velocity distributions of the MCSs in the strengthening and weakening stages of the four periods of convective activity, to reflect their dynamic variation. As can be seen, there was a prominent characteristic of upper level (lower level) positive (negative) divergence in the cloud area of MCSs during the strong development period, and this was not only a dynamic characteristic of the MCSs but also of the rainstorm produced. At 1800 UTC 8 September, during the first period of convection, there was negative divergence up to -4×10^{-5} s^{-1}, positive vorticity up to 7×10^{-5} s^{-1}, and vertical velocity up to -7×10^{-1} Pa s^{-1}. At 1800 UTC 10 September, during the second period of convection, the negative divergence reached -2×10^{-5} s^{-1}, the positive vorticity 4×10^{-5} s^{-1}, and the vertical velocity -3×10^{-1} Pa s^{-1}. At 1800 UTC 11 September, during the third period of convection, the negative divergence reached -2×10^{-5} s^{-1}, the positive vorticity 2×10^{-5} s^{-1}, and the vertical velocity -3×10^{-1} Pa s^{-1}. At 0000 UTC 13 September, during the fourth period of convection, the negative divergence reached -6×10^{-5} s^{-1}, the positive vorticity 13×10^{-5} s^{-1}, and the vertical velocity -6×10^{-1} Pa s^{-1}. The variation in these physical parameters demonstrates that the MCSs of the second period were stronger than those during the first stage and, correspondingly, the SN for large rainstorms was the highest. In the weakening period, the characteristic of upper

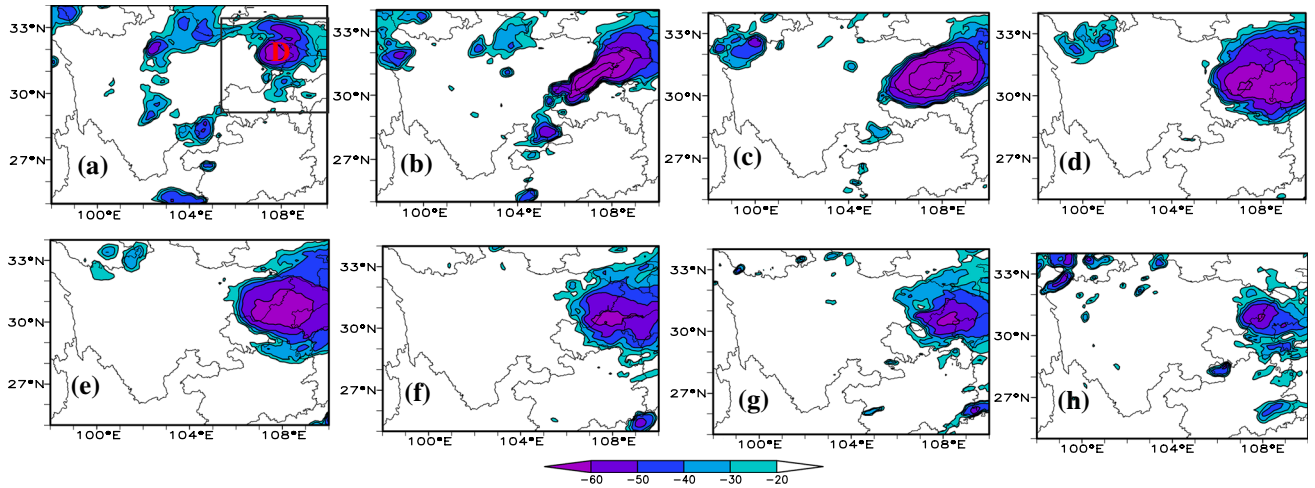

Fig. 6 Tb distribution in the fourth period of MCS activity (units: °C) at **a** 1600 UTC 12 September, **b** 1900 UTC 19 September, **c** 2100 UTC 12 September, **d** 0000 UTC 13 September, **e** 0200 UTC 13 September, **f** 0500 UTC 13 September, **g** 0700 UTC 13 September, and **h** 1000 UTC 13 September

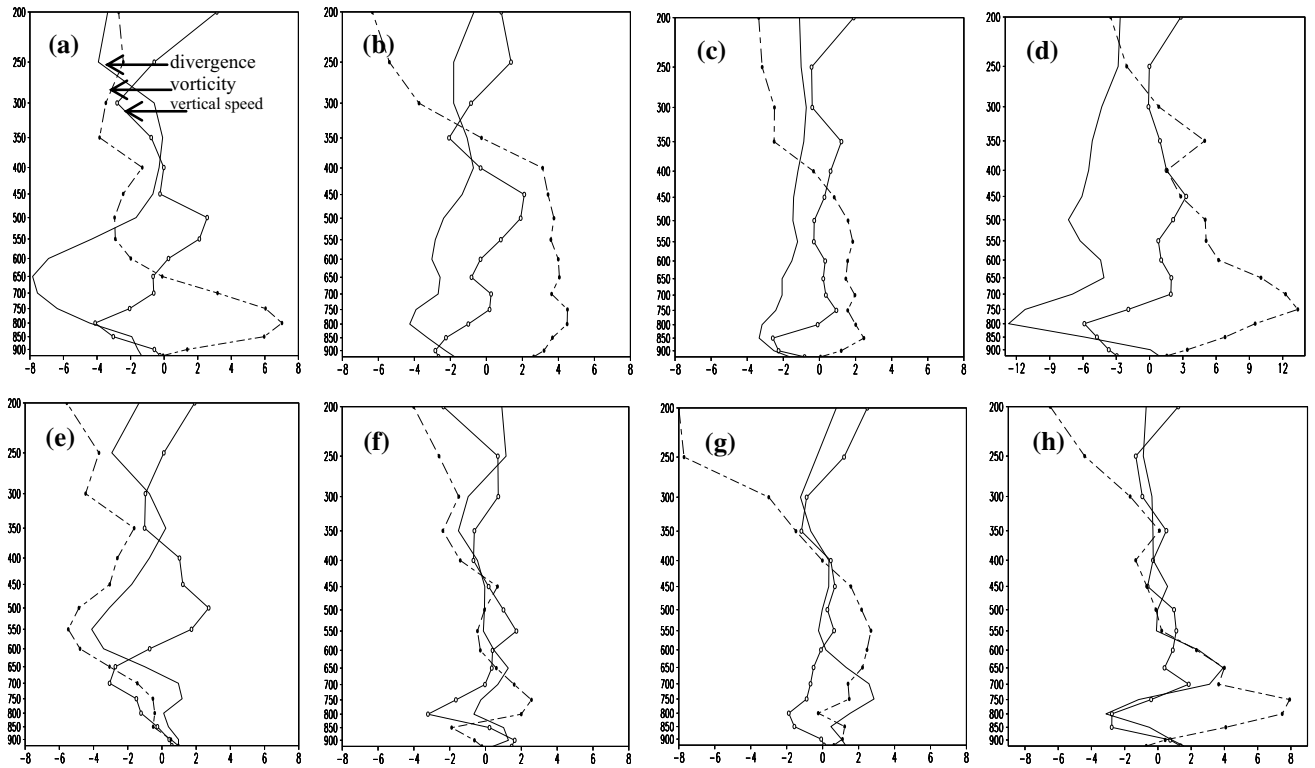

Fig. 7 Vorticity, divergence (units: 10^{-5} s^{-1}), and vertical velocity (units: 10^{-1} Pa s^{-1}) based on NCEP_fnl data in the MCSs **a**–**d** developing and **e**–**h** weakening periods: **a** 1800 UTC 08 September (105°E, 31°N); **b** 1800 UTC 8 September (105°E, 31°N); **c** 1800 UTC 11 September (106°E, 31°N); **d** 0000 UTC 13 September (107°E; 31°N); **e** 0000 UTC 9 September (107°E, 32°N); **f** 0600 UTC 11 September (107°E, 32°N); **g** 0600 UTC 12 September (108°E, 32°N); **h** 1200 UTC 13 September (108°E, 31°N)

level (lower level) positive (negative) divergence was not so prominent. In the first stage of convection (Fig. 7e–g), the vertical speed had been converted to a weak sinking airflow, the vertical thickness of PV and negative divergence became thinner, and the Tb increased markedly. In the fourth period of convection (Fig. 7h), although the lower layer retained the shallow characteristics of positive vorticity and negative divergence, the MCSs had further weakened.

Therefore, an adjustment of upper level (lower level) positive (negative) divergence was clear during the periods of MCS enhancement and weakening. In addition, it demonstrated that if the configuration of a weather system can establish such a dynamic structure of upper level (lower level) positive (negative) divergence, it will certainly play a positive role in the activities of MCSs, and the result is consistent with the study of Chen and Li (2013). In this study, we were more interested in what the differences were in terms of the physical conditions and the positive effects on MCS activity between the BIT and BLV situations. These aspects are discussed next.

5 Analysis of the differences in conditions between the BIT and BLV

5.1 Configuration differences among the impacting systems

Because of the sparseness of sounding data and difficultly in calculating the necessary physical quantities, it was necessary to use a different data source. After comparison with sounding data, we were confident that NCEP_fnl offered a good reflection of the circulation characteristics of the BIT and BLV. Meanwhile, taking into account the consistency of the atmospheric circulation on each day during the first stage, we analyzed the circulation based on average composites of the BIT and BLV, separately. In the second stage, because of the constant SWCV, we only selected a part of the period as representative for the analysis.

The elements of atmospheric circulation analyzed in the upper layer (150-hPa geopotential height and positive divergence), middle layer (588-gpdam WPSH), and lower layer (850-hPa wind and negative divergence) were chosen to reflect the configuration differences between the BIT and BLV (Fig. 8). When the BIT was evolving toward the BLV (Fig. 8a, b), the 150-hPa geopotential height of the South Asian high reached 1438 gpdam, and the divergent area was in the rainstorm zone, superimposed on the negative divergence area at 850 hPa. The structure of the upper level (lower level) positive (negative) divergence was formed, with the 500-hPa WPSH at the eastern edge of the basin and its 588-gpdam line being abnormally stable. When the BLV evolved toward the BIT (Fig. 8c, d), the geopotential height values of the SAH were 1436–1438 gpdam; the upper level divergent area was south of 31°N, but the lower level convergence zone was north of 31°N; and the position of the upper level (lower level) positive (negative) divergence tended to coincide, recommencing the development of MCSs. In the BLV activity of the second stage (Fig. 8e, f), the convective activity was the strongest, as was its rainstorm, corresponding to the structure of upper level (lower level) positive (negative) divergence being significantly enhanced; for instance, the upper level positive divergence value was greater than 7×10^{-5} s^{-1} and the lower level negative convergence value was less than -2.5×10^{-5} s^{-1}, which was conducive to an enhancement of the "suction effect" of the atmosphere. Therefore, stimulated by the configuration of the weather systems, the structure of the upper level (lower level) positive (negative) divergence was very clear throughout the rainstorm process.

To further understand the airflow structure in the vertical direction, we took both a warped (figure omitted) and zonal vertical profile along (106°E, 32°N) and discovered that there was rising airflow in the rainstorm area. In addition, the following characteristics along the vertical profile at 32°N (Fig. 9) were found: In the first stage of alternating evolution of the BIT (Fig. 9a, b) and BLV (Fig. 9c, d), there was a zonally vertical circulation of clockwise rotation in the lower layer and its ascending branch was located along 104°–107°E. From the vertical helicity and vertical velocity distribution, their values in the BIT situation were slightly larger than those in the BLV situation; for instance, vertical velocity reached 3×10^{-1} Pa s^{-1} and vertical helicity reached 50×10^{-6} Pa s^{-2} to 20×10^{-6} Pa s^{-2} in the BIT period, and vertical velocity reached 3×10^{-1} Pa s^{-1} and vertical helicity reached 30×10^{-6} Pa s^{-2} to 20×10^{-6} Pa s^{-2} in the BLV period. Therefore, the numerical values and temporal evolution of MCS intensity were highly consistent; that is, when vertical helicity and vertical velocity were large, the convection was more vigorous. In the BLV of the second stage (Fig. 9e, f), the upward branch of the zonal circulation was deeper and reached 300 hPa, the vertical velocity value was below -9×10^{-1} Pa s^{-1}, and the vertical helicity value was 50×10^{-6} Pa s^{-2}. During this period, the convective cloud was larger and deeper.

Clearly, the main difference between the configuration of the BIT and BLV was that there was a structure of upper level (lower level) positive (negative) divergence in the BIT of the first stage, and the VH in the upward branch of the zonal vertical circulation was larger compared with in the BLV period, meaning that the MCSs developed strongly in the BIT period. In the second stage, the structure of the upper level (lower level) positive (negative) divergence further enhanced, and the vertical helicity in the upward branch of the zonal vertical circulation was significantly larger than that in the first stage, corresponding to the MCSs being at their strongest during the entire rainstorm phase. Therefore, the enhancement and weakening of MCSs was closely related to the dynamic adjustment of the weather systems and the upward branch of zonal vertical circulation in the rainstorm area.

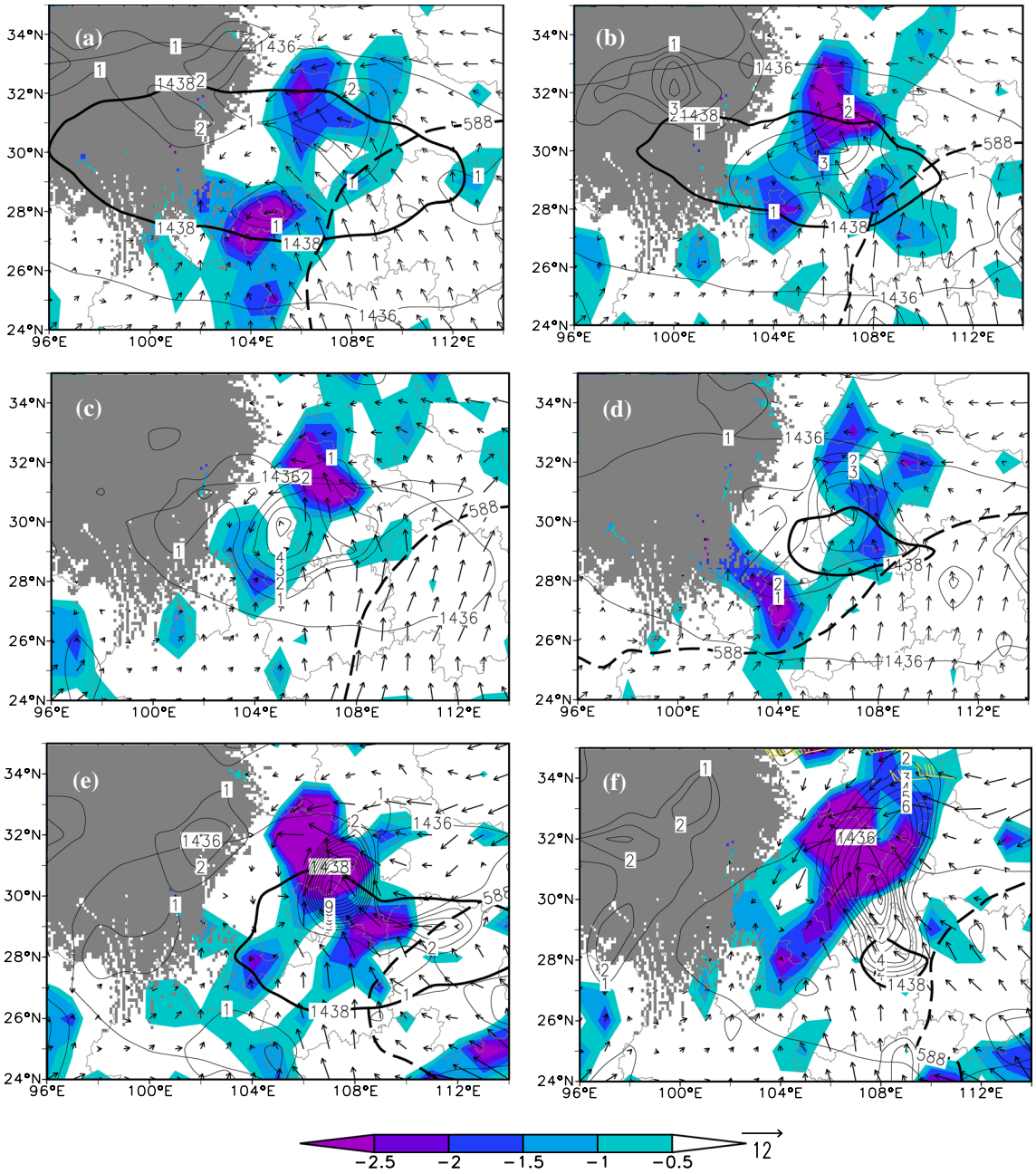

Fig. 8 150-hPa geopotential height field (solid line ≥ 1436 gpdam), wind field (≥ 30 m s^{-1}), and divergence (units: 10^{-5} s^{-1}), 588-gpdam line of the 500-hPa WPSH, 850-hPa wind vector (units: m s^{-1}), and divergence (shaded area; units: 10^{-5} s^{-1}) based on NCEP_fnl data: **a** average composite during 1200 UTC 8–11 September; **b** average composite during 1800 UTC 8–11 September; **c** average composite during 0000 UTC 9–12 September; **d** average composite during 0600 UTC 9–12 September; **e** 1800 UTC 12 September; **f** 0000 UTC 13 September

5.2 Sounding characteristics near the BIT and BLV

We used the sounding data at Wenjiang and Dazhou in the SB to analyze the convective environment of the first stage, and the sounding data at Chongqing for the second stage (Fig. 10). The data revealed a dry upper level and wet lower level structure in the vicinity of the BIT that was very obvious, as well as large convective available potential energy (CAPE) and unstable stratification. At 1200 UTC 8 September at the sounding station of Wenjiang (WJSS) (Fig. 10a, b), CAPE = 374.2 J kg^{-1} and precipitable water (PW) = 44.6 mm, unstable energy, and water vapor had increased (compared to 0000 UTC 8 September), *K*-index (KI) = 36 °C, and lifting index (LI) = − 0.33. At the

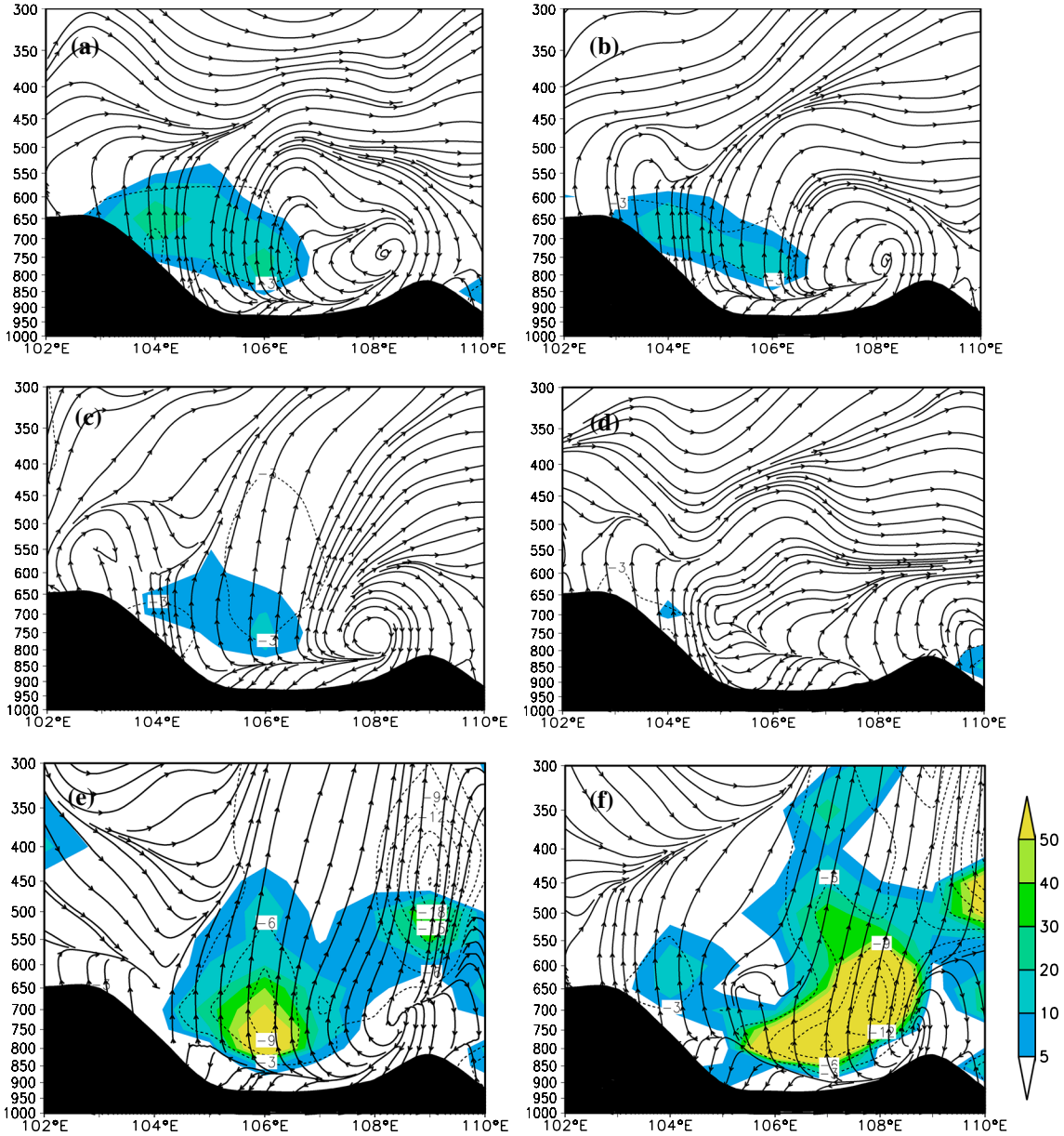

Fig. 9 As in Fig. 8 but for vertical helicity (shaded area; units: 10^{-6} Pa s^{-2}), vertical velocity (ω; dotted line; units: 10^{-1} Pa s^{-1}), and the composited circulation according to $\omega \times (-100)$ and u (zonal wind; units: m s^{-1}). **a**–**f** Depict the vertical section along 32°N based on NCEP_fnl data

sounding station of Dazhou (DZSS), CAPE = 3093.8 J kg^{-1}, PW = 52.6 mm and, compared to WJSS, the energy and water vapor of DZSS were higher, but the saturated wet layer was relatively thin and focused at 700 hPa. Therefore, in this favorable convective environment, a rainstorm emerged in the middle of the basin, and then the rainy area moved to the northeast of the basin. At 1200 UTC 10 September (Fig. 10c, d), the values of CAPE and PW were large at WJSS and DZSS, with the PW increasing significantly at WJSS and the CAPE increasing at DZSS. At 1200 UTC 11 September (Fig. 10e, f), the CAPE value reduced, PW values maintained above 50 mm, and the LI was negative. This meant that the lower level of the atmosphere was a favorable uplift environment and, once there were no longer any large CAPE values, severe ascending motion [$\omega_{max} \approx (2CAPE)^{1/2}$] would have arisen, providing favorable conditions for MCS growth. In addition, the dry upper level and wet lower level humidity structure was not obvious in the BLV situation; the occurrence of high CAPE at WJSS mainly occurred before

Fig. 10 Distribution of the *T*-log *P* chart near the **a**–**f** BIT and **g**–**h** BLV: **a**, **b** 1200 UTC 8 September; **c**, **d** 1200 UTC 10 September; **e**, **f** 1200 UTC 11 September; **g** 1200 UTC 12 September; **h** 0000 UTC 13 September ▶

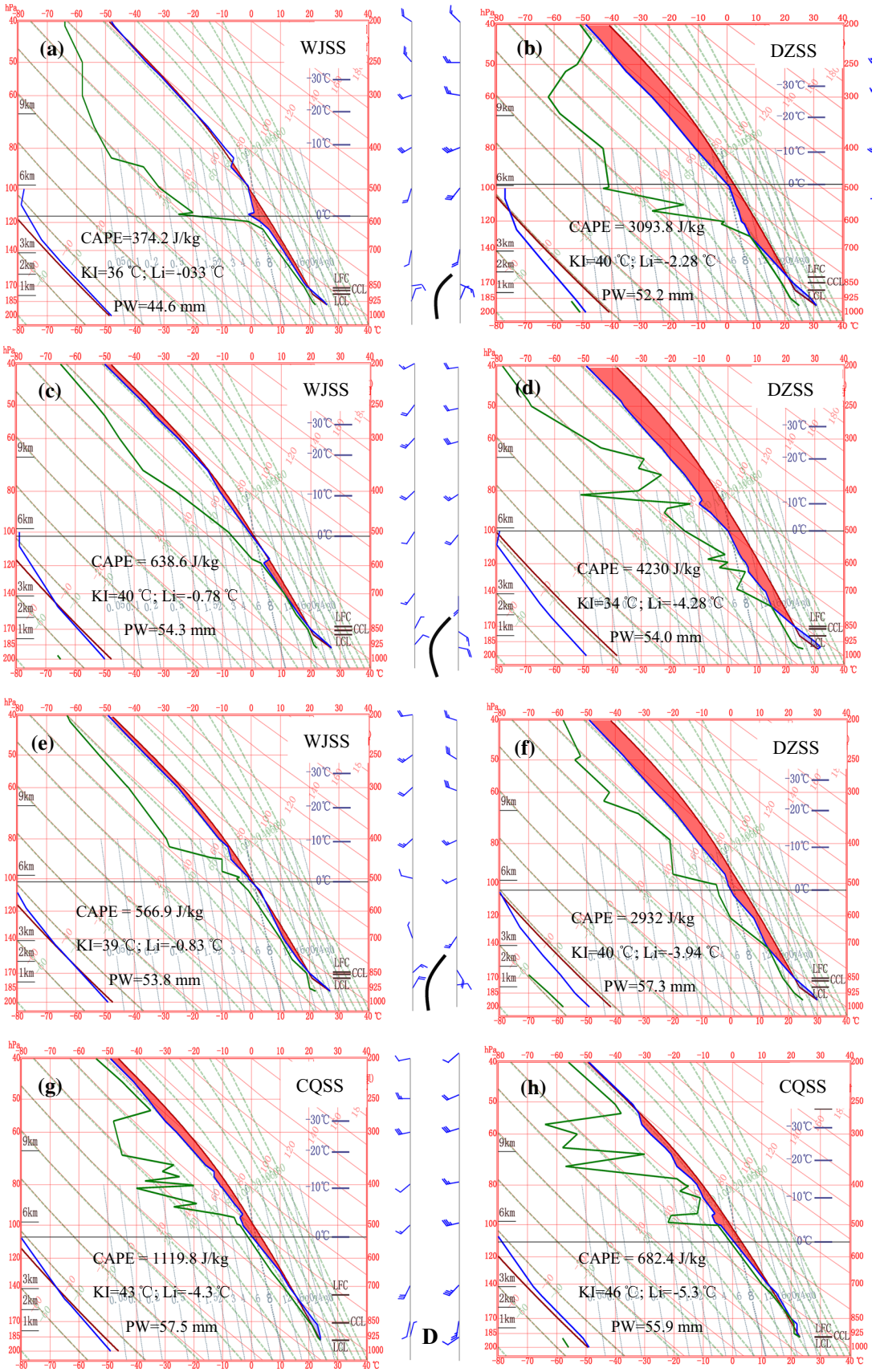
(a)
WJSS
CAPE=374.2 J/kg
KI=36 ℃; Li=-033 ℃
PW=44.6 mm
(b)
DZSS
CAPE = 3093.8 J/kg
KI=40 ℃; Li=-2.28 ℃
PW=52.2 mm
(c)
WJSS
CAPE = 638.6 J/kg
KI=40 ℃; Li=-0.78 ℃
PW=54.3 mm
(d)
DZSS
CAPE = 4230 J/kg
KI=34 ℃; Li=-4.28 ℃
PW=54.0 mm
(e)
WJSS
CAPE = 566.9 J/kg
KI=39 ℃; Li=-0.83 ℃
PW=53.8 mm
(f)
DZSS
CAPE = 2932 J/kg
KI=40 ℃; Li=-3.94 ℃
PW=57.3 mm
(g)
CQSS
CAPE = 1119.8 J/kg
KI=43 ℃; Li=-4.3 ℃
PW=57.5 mm
D
(h)
CQSS
CAPE = 682.4 J/kg
KI=46 ℃; Li=-5.3 ℃
PW=55.9 mm

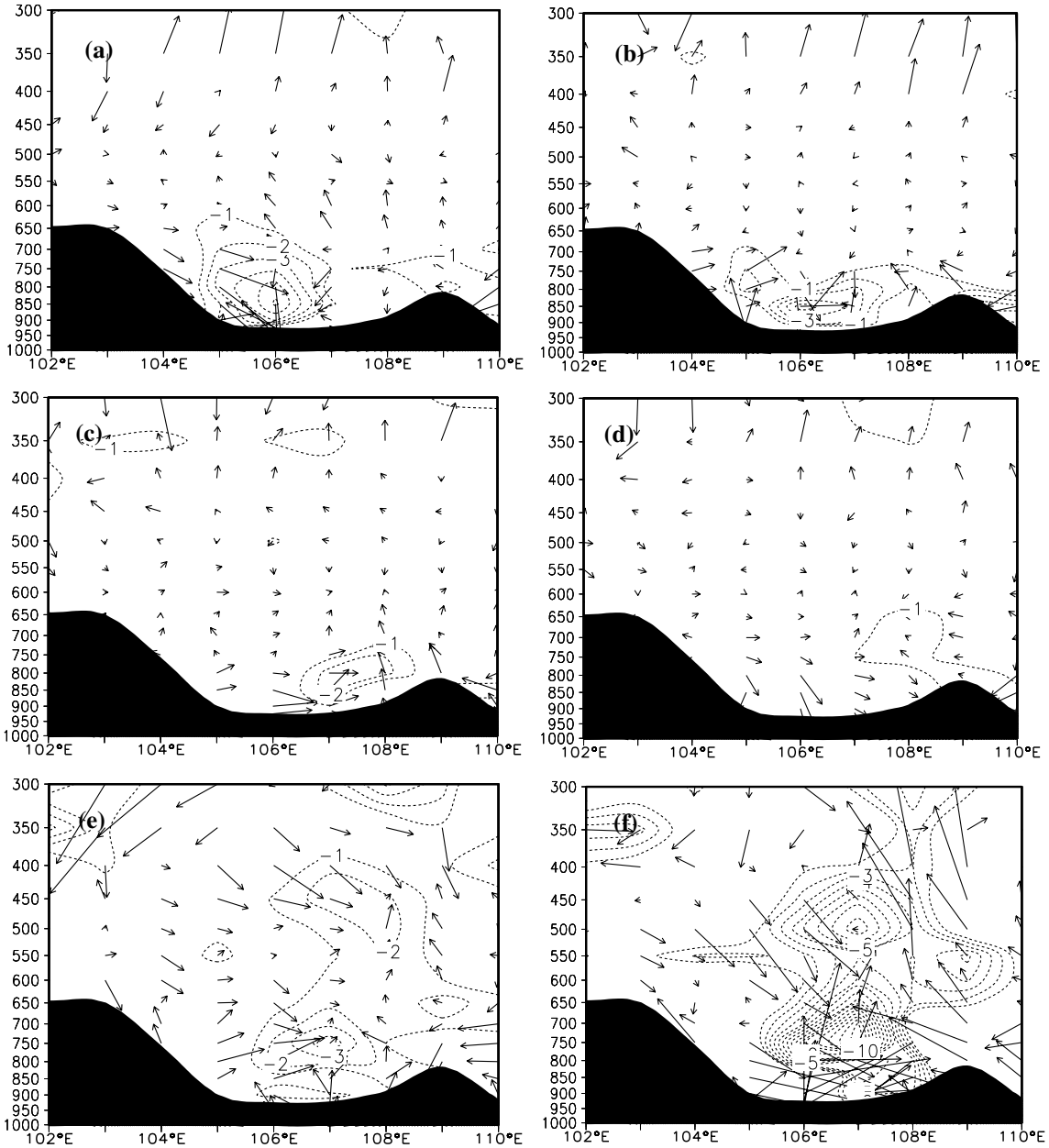

Fig. 11 As in Fig. 9 but for the wet Q-vector (units: 10^{-11} m hPa^{-1} s^{-2}) and its divergence (units: 10^{-16} hPa^{-1} s^{-3}) distribution based on NCEP_fnl data

1200 UTC 9 September, with the values from 0000 UTC 10 September to 1200 UTC 12 September being close to zero. Although the CAPE value at DZSS existed at 0800 UTC, compared to those at 1200 UTC, they were smaller. Therefore, from the convective environment of the sounding chart, the differences in physical conditions between 1200 UTC and 0800 UTC were that the CAPE values and humidity structure (i.e., dry upper level and wet lower level) were more favorable in the BIT situation.

In terms of the sounding physical quantities of the second stage, the sounding station at Chongqing (CQSS) was taken as the representative station for analysis (Fig. 10g, h). Compared to the low vortex environment of the first stage, the sounding physical quantities were more conducive to the development of MCSs, because a dry upper level and wet lower level structure was again observed, along with large CAPE values, PW values greater than 50 mm, and KI values above 40 °C. Clearly, in both the BLV or BIT situation, if the above characteristics in terms of sounding physical quantities are observed, strong MCS activity will occur. Therefore, this humidity structure (i.e., dry upper level and wet lower

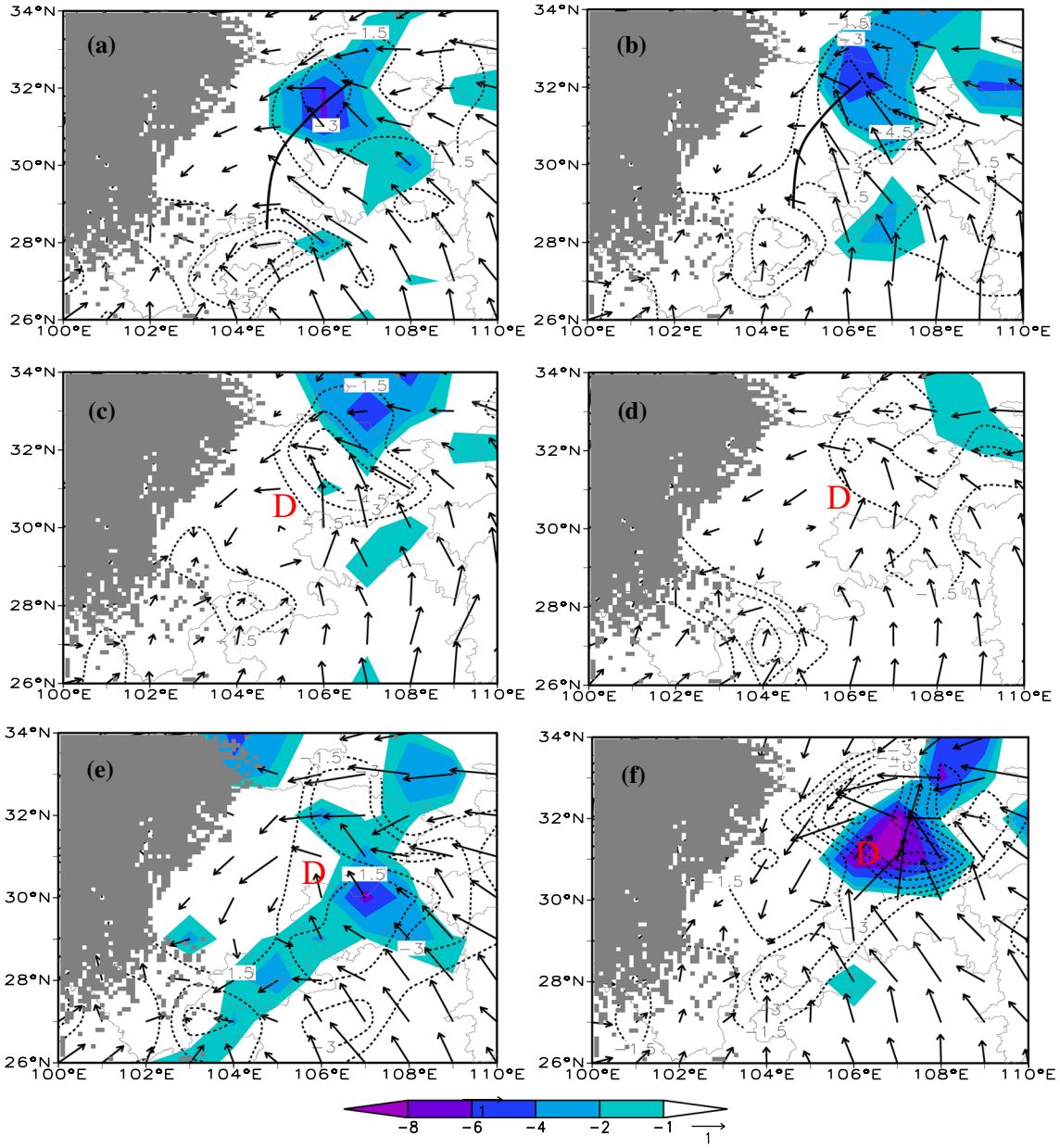

Fig. 12 Vectors (units: kg m^{-1} hPa^{-1} s^{-1}) and divergence (10^{-5} kg m^{-2} hPa^{-1} s^{-1}) of 850-hPa water vapor flux and wet Q-vector divergence (shaded area; units: 10^{-16} hPa^{-1} s^{-3}) based on NCEP_fnl data, in which the arrow is the water vapor flux vector, the dashed line is the divergence of water vapor flux, and "D" is the BLV: **a**, **b** BIT in the first stage; **c**, **d** BLV of the first stage; **e**, **f** BLV of the second stage

level) and the occurrence of large CAPE can be used as an important basis for judging the development of convection.

5.3 Local forcing effect for ascending motion

The above analysis shows that there were favorable thermodynamic conditions for convection—and especially, strong ascending motion was necessary. In this next part of the study, we used a diagnostic quantity (non-geostrophic wet Q-vector; NGWQV) to analyze the ascending motion.

Regarding the Q-vector, its concept was first proposed by Hoskins et al. (1978), who deduced the ω equation of the Q-vector divergence expression. Then, much later, Davis-Jones (1991) developed a generalized Q-vector ($\vec{Q}^*$) and deduced the ω equation of the $\vec{Q}^*$ divergence expression. However, these Q-vectors are only obtained under the assumed condition that the atmosphere is adiabatic, when, in fact, the atmosphere is non-adiabatic in the process of the condensation latent-heat release of precipitation. To further consider the condensation latent heat of the atmosphere,

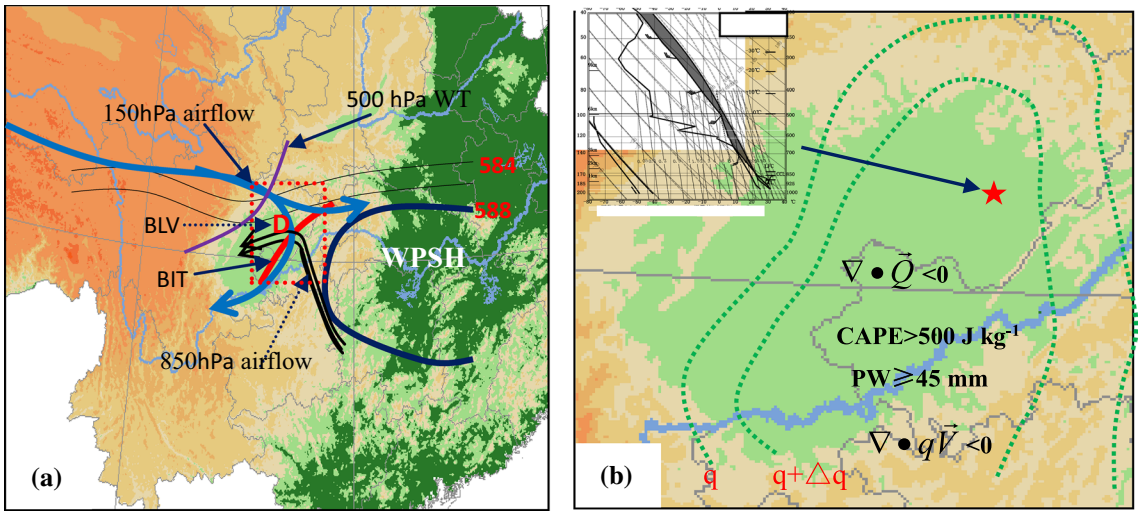

Fig. 13 Schematic illustrations of the **a** weather system configuration and **b** corresponding environmental field for the occurrence of the rainstorm. Depicted in **a** is the 150-hPa airflow (≥ 30 m s^{-1}), 850-hPa airflow (≥ 10 m s^{-1}), and 500-hPa WT (westerly trough); "D" is the BLV or SWCV. Depicted in **b** is the q (specific humidity), the $\nabla \cdot \vec{Q}$ (divergence of the wet Q-vector), CAPE, PW, and $\nabla \cdot q\vec{V}$ (convergence of water vapor flux)

Zhang (1998) deduced the NGWQV expression, and then, Yue and Shou (2008), Yue et al. (2003, 2015) used it to diagnose the heavy rain area and provide a modified expression.

According to the formulation [Eq. (6)] of the non-geostrophic ω equation, its forcing item is the wet Q-vector (Zhang 1998):

$$\nabla^2(\sigma\omega) + f^2\frac{\partial^2\omega}{\partial p^2} = -2\nabla \cdot \vec{Q}^*. \tag{6}$$

When the omega field shows a wave feature, the following can be obtained:

$$\nabla^2(\sigma\omega) \propto -\omega. \tag{7}$$

Equation (7) can be used to diagnose the vertical motion as follows: if $\nabla \cdot \vec{Q}^* < 0$ ($\nabla \cdot \vec{Q}^* > 0$), then $\omega < 0$ ($\omega > 0$), which is conductive to ascending (descending) motion. Figure 11 shows the NGWQV and its divergence profile along 32°N, from which it can be seen that, for either BIT or BLV circulation, the wet Q-vector divergence along 105°–108°E was negative at the low level, and its vector direction points to the ascending branch of zonal vertical circulation. Compared to the vertical velocity (dotted line in Fig. 9), the negative divergence region of the wet Q-vector and the region of vertical velocity were basically the same, albeit with differences in terms of their vertical position. In the first stage, the negative divergence of the wet Q-vector (Fig. 11a, b) in the BIT circulation was very similar in terms of height as the vertical velocity (Fig. 9a, b), whereas the negative divergence of the wet Q-vector (Fig. 11c, d) in the BLV circulation was not (Fig. 9c, d). For instance, at 0000 UTC 9–12 September, the average vertical velocity was mainly within 700–450 hPa, whereas the negative divergence of the wet Q-vector was mainly below 700 hPa. At 0600 UTC 9–12 September, the average vertical velocity was very small and the negative divergence of the wet Q-vector was mainly below 650 hPa. In the second stage, the negative divergence of the wet Q-vector enhanced and its center values exceeded 10×10^{-16} hPa^{-1} s^{-3}. In the ascending branch of the zonal vertical circulation, the characteristic of deep negative divergence of the wet Q-vector was reflected and, up to 300 hPa and above, also had the same vertical height as the vertical velocity (Fig. 9e, f). This indicates that when the negative divergence of the wet Q-vector is superimposed on the vertical ascending velocity, the convective development of the rainstorm area is favored. On the contrary, if the negative divergence of the low-level NGWQV is weak and does not superimpose on the vertical velocity, the convection is weakened or not obvious. This reflects the importance of negative divergence Q-vectors in a rainstorm of this type.

In addition, in longer rainstorm weather, water vapor is an important condition—in particular, its convergence is essential in the forced ascending motion area. Figure 12 further analyzes the relationship between the 850-hPa water vapor and the wet Q-vector convergence zone, wherein Fig. 12a–d represents the wet Q-vector divergence and water vapor transport in the BIT and BLV of the first stage, respectively. Figure 12e, f, meanwhile, represents the wet Q-vector divergence and water vapor transport in the BLV of the second stage. The water vapor flux vector is evident from south to north, forming a water vapor flux zone during the BIT, and is

transported by the southeasterly wind. The water vapor convergence zone and wet Q-vector divergence negative zone are basically coincident, and this would have been highly favorable for the convective development of wet air. During the BLV period, the convergence of water vapor was weakened and was inconsistent with the negative divergence zone of the wet Q-vector, which was not conducive to the development of strong precipitation.

In the second stage, the convergence of water vapor flux and wet Q-vector divergence were stronger than those in the first stage, thus creating a stronger rainstorm. This indicates that, in the area where low-level water vapor convergence is significant, if a low-level forced uplift effect emerges, it will cause more favorable convective activity to develop. On the other hand, it is also shown that, in this particular case, one of the main reasons for the reduction in BLV precipitation in the first three periods of convection, and the enhancement of BLV precipitation in the fourth period of convection, was that the convergence and forced uplift effect of the low-level water vapor changed significantly.

6 Conclusions and discussion

(1) Against a stable large-scale circulation background, the rainstorm investigated in the present study was caused by MCSs induced by the alternating evolution of an inverted trough (i.e., the BIT) and a southwest vortex (i.e., the BLV), and four periods of convective activity were observed. During the first stage of heavy rain (1200 UTC 8 September to 0000 UTC 12 September), which encompassed the first three periods of convective activity, MCSs enhanced in the BIT and weakened in the BLV. The second stage of the storm (0000 UTC 12 September to 0000 UTC 14 September), comprising the fourth period of convective activity, was caused by the MCSs induced by the BLV. During the activity of the MCSs, there were obvious cold cloud areas and Tb values below − 60 °C in the mature stage. In the cloud area, the MCSs typically showed characteristics of upper level (lower level) positive (negative) divergence and the vertically ascending airflow which was deep, which was not only the driving force for the maintenance of the MCSs but also one of the mechanisms that produced rainstorms.

(2) The enhancement and weakening of the MCSs was closely related to the dynamic adjustment of weather systems and the upward branch of zonal vertical circulation in the rainstorm area. When the MCSs developed strongly, the characteristic of upper level (lower level) positive (negative) divergence was more obvious and the vertical helicity values were larger compared with the weakening period. Meanwhile, the stratification reflected by the sounding chart indicated that larger CAPE values and a dry upper level and wet lower level humidity profile were an important cause of convective development. When the lower layer of the atmosphere was in the negative divergence of the non-geostrophic Q-vector and water vapor convergence, the environment featuring unstable high energy and high humidity was conducive to inducing MCSs and causing rainstorms. Based on this analysis, a conceptual model of the occurrence of this rainstorm was produced (Fig. 13). In addition to focusing on the stability of the weather systems, we also analyzed the upper level divergence zone and lower level convergence zone. The divergence zone of the upper layer (Fig. 13a) was often observed near a significant streamline divergence zone on the weather map, and the convergence zone of the lower layer was positioned where the lower level wind vector turned obviously and at the intersection with prominent upper level airflow. Furthermore, there was a dry upper level and wet lower level humidity structure, along with larger CAPE values (CAPE > 500 J kg^{-1}, in this case), and the lower level physical quantities satisfied the following diagnosis: $\nabla \cdot \vec{Q} < 0$; PW ≥ 45 mm. Where these conditions were met was usually the rainstorm area.

(3) In terms of the rainstorm forecast, the most overlooked aspect was the importance of the evolution of the BIT. In heavy rainfall events in the Sichuan region, cases caused by low vortices (i.e., southwest vortices and Tibetan Plateau vortices) are very common. However, beyond this, it is necessary to distinguish the relationship between the low vortex and the rainstorm; that is, the low vortex being generated in the rainstorm or its activity causing the rainstorm. In the present rainstorm case, the low vortex of the first stage generated after the rainstorm, but a strong low vortex caused the rainstorm during the precipitation process. Compared to the traditional low vortex rainstorm forecasts, there are both universality and individuality.

Acknowledgements This work was supported by a key project of the National Natural Science Foundation of China (No. 91337215). We are grateful to the strong convection forecasting team at the CMA for the assistance which they provided.

References

Bei NF, Zhao SX, Gao ST (2002) Numerical simulation of a heavy rainfall event in China during July 1998. Meteorol Atmos Phys 80(1–4):153–164. https://doi.org/10.1007/s007030200022

Chen YR, Li YQ (2013) Characteristics of mesoscale convective system and its effects on short-time severe rainfall in Sichuan Basin

during 21–22 July 2012. Meteorol Mon 39(7):848–860. https://doi.org/10.7519/j.issn.1000-0526.2013.07.006 **(in Chinese)**

Chen LS, Luo ZX (2003) A preliminary study of the dynamics of eastward shifting cyclonic vortices. Adv Atmos Sci 20:323–332. https://doi.org/10.1007/BF02690790

Chen YR, Li YQ, Zhao TL (2015) Cause analysis on eastward movement of Southwest China vortex and its induced heavy rainfall in South China. Adv Meteorol. https://doi.org/10.1155/2015/481735

Cheng MH, He HZ, Mao DY, Qi YJ, Cui ZH, Zhou FX (2001) Study of 1998 heavy rainfall over the Yangtze River Basin using TRMM data. Adv Atmos Sci 18(3):387–396. https://doi.org/10.1007/BF02919317

Cheng XL, Li YQ, Li Xu (2016) An analysis of an extreme rainstorm caused by the interaction of the Tibetan Plateau vortex and the Southwest China vortex from an intensive observation. Meteorol Atmos Phys 128(3):373–399. https://doi.org/10.1007/s00703-015-0420-2

Davis-Jones R (1991) The frontogenetical forcing of secondary circulations part I: the duality and generalization of the Q vector. J Atmos Sci. 48(4):497–509. https://doi.org/10.1175/1520-0469(1991)048<0497:TFFOSC>2.0.CO;2

Duan AM, Sun RZ, He JH (2017) Impact of surface sensible heating over the Tibetan Plateau on the western Pacific subtropical high: a land–air–sea interaction perspective. Adv Atmos Sci 34(2):157–168. https://doi.org/10.1007/s00376-016-6008-z

Feng XY, Liu CH, Fang GZ, Liu XD, Fang CY (2016) Climatology and structures of southwest vortices in the NCEP climate forecast system reanalysis. J Climate 29(21):7675–7701. https://doi.org/10.1175/JCLI-D-15-0813.1

Fu SM, Sun JH, Zhao SX, Li W (2011) The energy budget of a southwest vortex with heavy rainfall over South China. Adv Atmos Sci 28(3):709–724. https://doi.org/10.1007/s00376-010-0026-z

He ZW, Zhang QH, Sun J (2016) The contribution of mesoscale convective systems to intense hourly precipitation events during the warm seasons over central East China. Adv Atmos Sci 33(11):1233–1239. https://doi.org/10.1007/s00376-016-6034-x

Hoskings BJ, Dragchici I, Davies HC (1978) A new look at ω-equation. Q J R Meteorol Soc 104:31–38. https://doi.org/10.1002/qj.49710443903

Kuo YH, Cheng LS, Anthes RA (1986) Mesoscale analyses of the Sichuan flood catastrophe, 11–15 July 1981. Mon Weather Rev. 114(11):1984–2003. https://doi.org/10.1175/1520-0493(1986)114<1984:MAOTSF>2.0.CO;2

Kuo YH, Cheng LS, Bao JW (1988) Numerical simulation of the 1981 Sihuan flood. part I: evolution of a mesoscale southwest vortex. Mon Weather Rev. 116(12):2481–2504

Li GP, Deng J (2013) Atmospheric water monitoring by using ground-based GPS during heavy rains produced by TPV and SWV. Adv Meteorol. https://doi.org/10.1155/2013/793957

Li YQ, Gao WL (2007) Atmospheric boundary layer circulation on the eastern of Tibetan Plateau, China, in summer. Arct Antarct Alp Res 39(4):708–713

Li L, Zhang RH, Wen M (2011) Diagnostic analysis of the evolution mechanism for a vortex over the Tibetan Plateau in June 2008. Adv Atmos Sci 28(4):797–808. https://doi.org/10.1007/s00376-010-0027-y

Li L, Zhang RH, Wen M (2014a) Diurnal variation in the occurrence frequency of the Tibetan Plateau vortices. Meteorol Atmos Phys 125:135–144. https://doi.org/10.1007/s00703-014-0325-5

Li L, Zhang RH, Wen M et al (2014b) Effect of the atmospheric heat source on the development and eastward movement of the Tibetan Plateau vortices. Tellus A. https://doi.org/10.3402/tellusa.v66.24451

Li J, Du J, Zhang DL, Cui CG, Liao YS (2014c) Ensemble-based analysis and sensitivity of mesoscale forecasts of a vortex over southwest China. Q J R Meteorol Soc 140:766–782. https://doi.org/10.1002/qj.2200

Li YQ, Yu L, Chen BD (2015) An Assessment of design of observation network over the Tibetan Plateau based on observing system simulation experiments (OSSE). J Meteorol Soc Jpn 93(3):343–358. https://doi.org/10.2151/jmsj.2015-019

Lilly DK (1986) The structure and propagation of rotation convective storm. Part 2: helicity and storm. J Atmos Sci. 43(2):126–140. https://doi.org/10.1175/1520-0469(1986)043<0126:TSEAPO>2.0.CO;2

Lin ZQ (2015) Analysis of Tibetan Plateau vortex activities using ERA-Interim data for the period 1979–2013. J Meteorol Res 29(5):720–734. https://doi.org/10.1007/s13351-015-4273-x

Lu JH (1986) Generality of the southwest vortex. China Meteorological Press, Beijing, pp 1–270 **(in Chinese)**

Lu HJ, Gao ST (2003) On the helicity and the helicity equation. Acta Meteorol Sin 61(6):684–691. https://doi.org/10.11676/qxxb2003.069 **(in Chinese)**

Ni CC, Li GP, Xiong XZ (2017) Analysis of a vortex precipitation event over Southwest China using AIRS and in situ measurements. Adv Atmos Sci 34(4):559–570. https://doi.org/10.1007/s00376-016-5262-4

Schumacher RS, Johnson RH (2005) Organization and environmental properties of extreme-rain-producing mesoscale convective systems. Mon Weather Rev 133:961–976. https://doi.org/10.1175/MWR2899.1

Schumacher RS, Johnson RH (2008) Mesoscale processes contributing to extreme rainfall in a midlatitude warm-season flash flood. Mon Weather Rev 136:3964–3986. https://doi.org/10.1175/2008MWR2471.1

Shen RJ, Reiter ER, Bresch JF (1986) Numerical simulation of the development of vortices over the Qinghai-Xizang Plateau. Meteorol Atmos Phys 35(1–2):70–95. https://doi.org/10.1007/BF01029526

Sun JH, Zhao SX, Xu GK, Meng QT (2010) Study on a mesoscale convective vortex causing heavy rainfall during the Mei-yu season in 2003. Adv Atmos Sci 27(5):1193–1209. https://doi.org/10.1007/s00376-009-9156-6

Tao SY, Ding YH (1981) Observational evidence of the influence of the Qinghai-Xizang (Tibet) Plateau on the occurrence of heavy rain and severe convective storms in China. Bull Am Meteorol Soc. 62:23–30. https://doi.org/10.1175/1520-0477(1981)062<0023:OEOTIO>2.0.CO;2

Wang B (1987) The development mechanism for Tibetan Plateau warm vortices. J Atmos Sci. 44:2978–2994. https://doi.org/10.1175/1520-0469(1987)044<2978:TDMFTP>2.0.CO;2

Wang Z, Gao K (2003) Sensitivity experiments of an eastward-moving southwest vortex to initial perturbations. Adv Atmos Sci 20(4):638–649. https://doi.org/10.1007/BF02915507

Wang B, Orlanski I (1987) Study of a heavy rain vortex formed over the eastern flank of the Tibetan Plateau. Mon Weather Rev. 115(7):1370–1393. https://doi.org/10.1175/1520-0493(1987)115<1370:SOAHRV>2.0.CO;2

Wang QW, Tan ZM (2014) Multi-scale topographic control of southwest vortex formation in Tibetan Plateau region in an idealized simulation. J Geophys Res 119(20):11543–11561. https://doi.org/10.1002/2014JD021898

Wu GX, Chen SJ (1985) The effect of mechanical forcing on the formation of a mesoscal vortex. Q J R Meteorol Soc 111:1049–1070. https://doi.org/10.1002/qj.49711147009

Xiang SY, Li YQ, Li D, Yang S (2013) An analysis of heavy precipitation caused by a retracing plateau vortex based on TRMM data. Meteorol Atmos Phys 122:33–45. https://doi.org/10.1007/s00703-013-0269-1

Yu SH, Gao WL (2009) Large-scale conditions of Tibet Plateau vortex departure. Sci Cold Arid Reg 1:559–569

Yu SH, Gao WL, Peng J, Xiao YH (2014) Observational facts of sustained departure plateau vortexes. J Meteorol Res 28(2):296–307. https://doi.org/10.1007/s13351-014-3023-9

Yu SH, Gao WL, Xiao DX, Peng J (2016) Observational facts regarding the joint activities of the southwest vortex and plateau vortex after its departure from the Tibetan Plateau. Adv Atmos Sci 33(1):34–46. https://doi.org/10.1007/s00376-015-5039-1

Yue CJ, Shou SW (2008) A modified moist ageostrophic Q vector. Adv Atmos Sci 25(6):1053–1061. https://doi.org/10.1007/s00376-008-1053-x

Yue CJ, Shou SW, Lin KP, Yao XP (2003) Diagnosis of the heavy rain near a Mei-yu front using the wet Q vector partitioning method. Adv Atmos Sci 20(1):37–44. https://doi.org/10.1007/BF03342048

Yue CJ, Gao ST, Liu L, Li XF (2015) A diagnostic study of the asymmetric distribution of rainfall during the landfall of typhoon Haitang (2005). Adv Atmos Sci 32(10):1419–1430. https://doi.org/10.1007/s00376-015-4246-0

Zhang XW (1998) An expression of the wet Q vector and application. Meteorol Mon 24(8):3–7 **(in Chinese)**